



Title	Aerodynamic-Heating Analysis of Sample-Return Capsule in Future Trojan-Asteroid Exploration
Author(s)	Takahashi, Yusuke; Yamada, Kazuhiko
Citation	Journal of thermophysics and heat transfer, 32(3), 547-559 <a href="https://doi.org/10.2514/1.T4837">https://doi.org/10.2514/1.T4837</a>
Issue Date	2018-07
Doc URL	<a href="http://hdl.handle.net/2115/71226">http://hdl.handle.net/2115/71226</a>
Rights	© 2018 American Institute of Aeronautics and Astronautics
Type	article (author version)
File Information	paper_hvrc.pdf



[Instructions for use](#)

# Aerodynamic Heating Analysis of Sample Return Capsule in Future Trojan Asteroid Exploration

Yusuke Takahashi<sup>1</sup>

*Hokkaido University, Kita 13 Nishi 8, Kita-ku, Sapporo, Hokkaido, 060-8628, Japan,*  
and

Kazuhiko Yamada<sup>2</sup>

*Japan Aerospace Exploration Agency, 3-1-1 Yoshinodai Chuo-ku, Sagami-hara, Kanagawa  
252-5210, Japan*

## Abstract

In sample return missions, the reentry velocity of a sample return capsule (SRC) is expected to be approximately 15 km/s; however, the reentry velocity of the Hayabusa SRC was 11.8 km/s. Strong aerodynamic heating caused by a high velocity can damage the capsule during reentry. To overcome this, two designs of high-velocity reentry capsules (HVRCs) were proposed. In one design, a rigid flare was attached to decrease the ballistic coefficient by increasing the front projected area. In the other design, the conventional Hayabusa SRC was used with no modifications. In this study, the aerodynamic heating of the HVRCs and the Hayabusa SRC were analyzed using numerical simulations. Plasma flow in the shock layer at the front of the capsules and expansion flow in the wake region around the capsules were investigated. The profiles of convective and radiative heat fluxes on the surfaces of these capsules were predicted. The heat fluxes at the stagnation points predicted by the present numerical simulation were in good agreement with that of the empirical models. At the strongest aerodynamic heating altitude, the total heat fluxes at the rear of the HVRCs and the Hayabusa SRC were approximately 2% of those in front of the capsules.

## Nomenclature

$a$	=	model parameter
$A$	=	area, m <sup>2</sup>
$B$	=	blackbody function, W/m <sup>3</sup>
$B_C$	=	ballistic coefficient
$C$	=	mass fraction
$C_d$	=	drag coefficient
$D$	=	effective diffusion coefficient, m <sup>2</sup> /s
$f$	=	function
$h$	=	enthalpy, J/kg
$I$	=	radiation intensity, W/m <sup>3</sup>
$k$	=	Boltzmann constant, J/K
$Kn_{\text{GLL}}$	=	Gradient-length local Knudsen number
$m$	=	mass, kg
$M$	=	molar mass, kg/mol
$n$	=	normal direction coordinate, m
$N_A$	=	Avogadro constant, mol <sup>-1</sup>
$q$	=	heat flux, W/m <sup>2</sup>

---

<sup>1</sup>Assistant Professor, Faculty of Engineering; ytakahashi@eng.hokudai.ac.jp.

<sup>2</sup>Assistant Professor, Institute of Space and Astronautical Science.

$R_N$	=	nose radius, m
$s$	=	one-dimensional coordinate, m
$T$	=	temperature, K
$u, V$	=	velocity, m/s
$\gamma$	=	catalytic coefficient
$\theta$	=	angle, rad
$\kappa$	=	absorption coefficient, $\text{m}^{-1}$
$\lambda$	=	mean free path, m
$\rho$	=	density, $\text{kg}/\text{m}^3$
$\Omega$	=	solid angle, sr

### *Subscripts*

ele, e	=	electron
$i$	=	chemical species
rot, R	=	rotation
stag	=	stagnation
trs, T	=	translation
vib, V	=	vibration
w	=	wall
$\lambda$	=	wavelength
$\infty$	=	freestream

### *Superscripts*

conv	=	convection
rad	=	radiation

## 1 Introduction

Atmospheric reentry is one of the most critical phases in a sample return mission. During atmospheric reentry to Earth from an interplanetary transfer orbit, which is often used in sample return missions, the vehicle reenters at a speed of more than 11 km/s and a very strong shock wave is formed at its front. This high-kinetic-energy gas is transformed into thermal and chemical energy across the shock wave; then, gas heated in the shock layer becomes a plasma via dissociation and ionization reactions. Aerodynamic heating derived from the shock wave can damage the capsule during the reentry phase. Examples of sample return missions at high reentry velocity are Hayabusa [1, 2] by the Japan Aerospace Exploration Agency (JAXA) and Stardust [3, 4] by the National Aeronautics and Space Administration (NASA). Recently, a new mission for Jupiter Trojan asteroid exploration with a solar power sail was proposed by JAXA [5, 6]. Moreover, sample return missions from outer planets and their moons in the solar system have been proposed [7]. Johnston et al. [8] numerically investigated the aerodynamic heating environment around a reentry vehicle with a velocity of 16-22 km/s in the Earth reentry phase. For the Earth return duration of Jupiter Trojan asteroids exploration, a reentry velocity of approximately 15 km/s is expected. Additionally, a reduction in the weight of the thermal protection system (TPS) is required, because a weight limit is imposed on the capsule.

In the present study, to address this issue, two conceptual designs of HVRC are proposed,

based on the Hayabusa sample return capsule (SRC). One of the concepts involves reducing the aerodynamic heating to the same degree as Hayabusa SRC by adjusting the ballistic coefficient. This is done by attaching a rigid flare to the reentry capsule (HVRC with a rigid flare). The other concept involves using the conventional configuration of Hayabusa SRC without any major modifications (HVRC without rigid flare). Here, the ballistic coefficient,  $B_C$ , is defined by

$$B_C = \frac{m}{C_d A} \quad (1)$$

where  $m$ ,  $C_d$ , and  $A$  are the mass, drag coefficient, and characteristic area of the reentry capsule, respectively. Note that in general, as the ballistic coefficient decreases, the aerodynamic heating reduces with the enhancement of the aerodynamic deceleration at higher altitude. The low-ballistic-coefficient flight of the HVRC with rigid flare can reduce aerodynamic heating during atmospheric reentry in spite of the initially high reentry velocity. However, because an increase in size typically coincides with an increase in weight, the requirements for the weight of the capsule, particularly TPS, become restrictive. On the other hand, one advantage of the HVRC without the rigid flare is that we can use the data available such as the aerodynamic characteristics of the capsule obtained during the Hayabusa mission. However, because of the increase in the peak heat flux and the total heat load due to aerodynamic heating during reentry, it is likely that the TPS weight will increase. In either case, it is important to predict accurate aerodynamic heating and feedback in the capsule design and development processes. Analysis of flow fields around the two capsule types is expected to validate the physical and numerical models for high velocity reentry and elucidate the aerodynamic heating environment during reentry at high velocities.

The Hayabusa SRC is equipped with a carbon-phenolic ablator on its front and rear heat shields as a TPS. Because the front heat shield of the Hayabusa SRC was exposed to severe convective and radiative heat fluxes due to the strong shock wave, a thick ablator material was required. On the other hand, heat fluxes due to convection and radiation could be reduced on the rear-side heat shield, because plasma flow (heated in the shock layer) was rapidly rarefied with supersonic expansion when inflowing into the wake. This indicates the possibility of a reduction in weight of the TPS at the rear-side of the capsule. Thus, it is important to accurately predict the aerodynamic heating environment and minimize the use of TPS material in the rear heat shield (in addition to reducing that at the front).

To reproduce the aerodynamic heating environment at a reentry velocity of 15 km/s use of high enthalpy facilities, e.g., an arc-heated wind tunnel, a shock tunnel, and a hypersonic wind tunnel, is required; however, their use is difficult and costly. Recently, advancements have been made in the development of high-performance computers and algorithms for numerical simulation. Numerical prediction with computational fluid dynamics (CFD) approaches has become relatively low-cost and is a particularly effective tool at the initial stages of design and development of reentry capsules. The present research objective is to investigate the aerodynamic heating of the HVRC without/with a rigid flare at a reentry velocity of approximately 15 km/s. The aim is also to examine aerodynamic heating over the HVRC with a rigid flare in the low-density environment and over the HVRC without a rigid flare at a higher velocity and a lower altitude. However, there are several details that remain unclear when constructing an analysis model for the HVRCs, because of the very high velocity of reentry. Therefore, to validate the numerical analysis model used here, one additional objective of this research is to predict aerodynamic heating for the Hayabusa SRC.

## 2 Reentry Capsules

In this section, assumptions regarding capsule design for aerodynamic heating analysis are made. Then, the configuration and reentry trajectory of the HVRCs are determined based on Hayabusa SRC.

### 2.1 Configuration

The total weight of the Hayabusa SRC was 16.3 kg; the ablator material, which forms the TPS, accounted for 10.3 kg of the total weight. Hayabusa SRC had a diameter of 400 mm. The front nose radius of Hayabusa SRC was 200 mm; the half cone angle at the rear side was 45°, as shown in Fig. 1. The drag coefficient of the capsule during atmospheric reentry was set to 1.147. The initial reentry velocity and flight path angle were 11.65 km/s and 12.7°, respectively. The peak heat flux and total heat load were 15 MW/m<sup>2</sup> and 275 MJ/m<sup>2</sup>, respectively. The maximum deceleration of Hayabusa SRC during reentry was approximately 50 G.

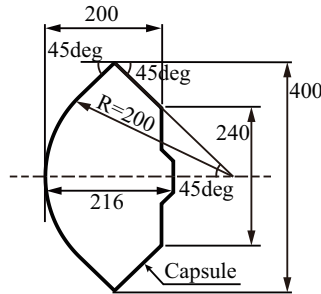


Figure 1: Schematic configuration of Hayabusa SRC and HVRC without rigid flare.

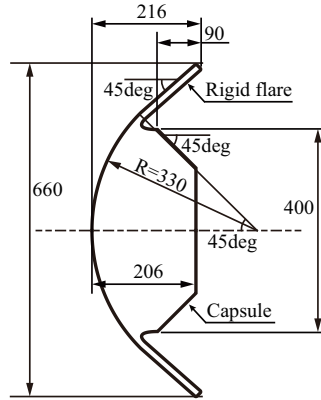


Figure 2: Schematic configuration of HVRC with rigid flare.

We calculate the convective and radiative heat fluxes using empirical formulas, i.e., the Detra-Kemp-Riddell [9] and Tauber-Sutton models [10], respectively, which are obtained in

units of  $\text{W}/\text{m}^2$

$$q_{\text{DKR}}^{\text{conv}} = \frac{110.35 \times 10^6}{\sqrt{R_N}} \sqrt{\frac{\rho_\infty}{1.225}} \left( \frac{V_\infty}{7924.8} \right)^{3.15} \left( \frac{h_{\text{stag}} - h_w}{h_{\text{stag}} - h_{w0}} \right), \quad (2)$$

$$q_{\text{TS}}^{\text{rad}} = 4.736 \times 10^8 R_N^a \rho_\infty^{1.22} f(V_\infty), \quad (3)$$

where  $R_N$ ,  $\rho_\infty$ ,  $V_\infty$ ,  $h_{\text{stag}}$ ,  $h_w$ , and  $h_{w0}$  are the noise radius, freestream density, freestream velocity, enthalpies at the stagnation point, hot wall, and cold wall, respectively. Here, the model parameter,  $a$ , in Eq. (3) is given by

$$a = 1.072 \times 10^6 V_\infty^{-1.88} \rho_\infty^{-0.325}, \quad (4)$$

and the function of the velocity  $f(V_\infty)$  is tabulated in Ref. [10].

In the design of reentry trajectories and configurations of HVRC, a constraint to maintain the same total weight (16.3 kg) and drag coefficient of the Hayabusa SRC is imposed. The reentry trajectory is obtained by solving an equation of motion for a point mass trajectory that considers the drag by the atmosphere and the gravity force exerting the capsule. A standard atmosphere model is used; however, wind is not considered. The initial reentry velocity is fixed at 14.5 km/s for the HVRCs. The flight path angle generally affects both the peak heat flux and the heat load due to aerodynamic heating. The peak heat flux becomes destructively large when the flight path angle becomes too large, whereas the capsule can be insufficiently decelerated when the flight path angle is too small. However, the angle between the two thresholds is arbitrarily selective.

The configuration of the HVRC without a rigid flare is set to be the same as that of Hayabusa SRC. For the HVRC without a rigid flare, the flight path angle is determined such that the maximum deceleration during reentry is the same as that of Hayabusa SRC (50 G). For this case, the flight path angle of the HVRC without a rigid flare becomes  $11.5^\circ$ . The peak heat flux at the stagnation point and heat load is expected to be approximately  $35 \text{ MW}/\text{m}^2$  and  $680 \text{ MJ}/\text{m}^2$ , respectively. This severe heating environment is resolved by increasing the thickness of the ablator. However, this increase causes problems: it increases the TPS weight and decreases the payload capacity for the HVRC without a rigid flare.

The basic configuration of the HVRC with a rigid flare is similar to that of Hayabusa SRC; however, it includes a flare on its capsule edge to increase the frontal projected area, as shown in Fig. 2. The size is determined based on conditions that the peak heat flux at stagnation and the total heat load during reentry are the same as those of Hayabusa SRC and minimization of the diameter of the capsule, in addition to the above-described constraints. For this case, the frontal projected diameter of the HVRC with the rigid flare is 660 mm and the flight path angle is  $11.4^\circ$ . The front nose radius is 330 mm. The peak heat flux and total heat load are  $15 \text{ MW}/\text{m}^2$  and  $273 \text{ MJ}/\text{m}^2$ , respectively.

The design parameters of the considered reentry capsule are summarized in Table 1. In this table, “case 1,” “case 2,” and “case 3” correspond to Hayabusa SRC, the HVRC without a rigid flare, and the HVRC with a rigid flare, respectively.

## 2.2 Reentry Trajectory

The reentry trajectories of Hayabusa SRC, the HVRC without a rigid flare, and the HVRC with a rigid flare are shown in Figs. 3(a), 3(b), and 3(c), respectively. The figures include profiles of convective and radiative heat fluxes at the stagnation point in front of the capsules during reentry, and the reentry velocity. The velocities of the HVRCs at the initial stage

Table 1: Design parameters of reentry capsules.

Capsule	Case 1	Case 2	Case 3
Reentry velocity, m/s	11,800	14,500	14,500
Flight path angle, ° (degrees)	12.7	11.5	11.4
Weight of capsule, kg	16.3	16.3	16.3
Diameter of capsule, mm	400	400	660
Front nose radius, mm	200	200	330

of reentry are set to 14.5 km/s. Because the ballistic coefficient of the HVRC with a rigid flare is lower, the capsule can decelerate at higher altitudes (compared to the reentry case for Hayabusa SRC and the HVRC without a rigid flare). The altitude at which the total heat flux reaches its peak value is approximately 64 km for the HVRC with a rigid flare, whereas the peak altitudes of aerodynamic heating for Hayabusa SRC and the HVRC without a rigid flare are approximately 52 km and 58 km, respectively. For the HVRC with a rigid flare, peak aerodynamic heating occurs in the low density environment at a high altitude. The radiative heat flux of Hayabusa SRC at stagnation is, at most, 20% of the total heat flux. On the other hand, the radiation values of the other HVRCs become larger than that of the Hayabusa SRC, which implies that prediction of radiation for the HVRCs is more important.

### 3 Analysis Model

In this section, the governing equations, physical models, and numerical methods for aerodynamic heating prediction (using CFD) used in this study are briefly described.

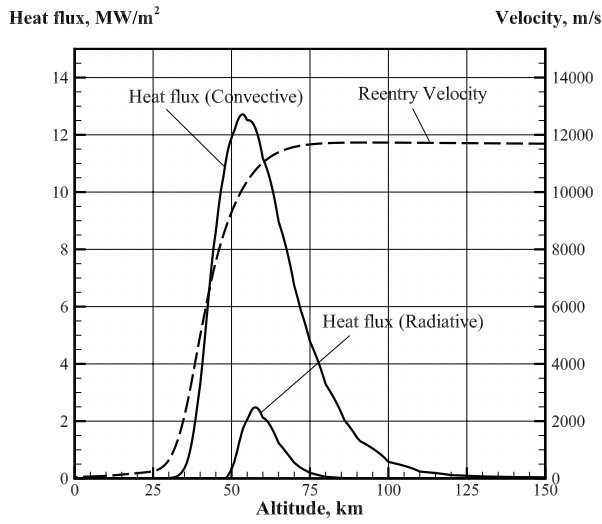
#### 3.1 Assumptions

In this study, the following assumptions are made. (1) The flow is laminar, axisymmetric, steady, and continuous. (2) The inflow gas is air. The ablator gas (including carbon and hydrogen systems) is not considered. (3) The flow field is in thermochemical non-equilibrium, and the temperature is separated into translational, rotational, vibrational, and electron temperatures. We assume that the electron-excitation energy and electron-energy modes are equilibrated. (4) The scattering of radiation is neglected. (5) The radiation is independent of temporal direction.

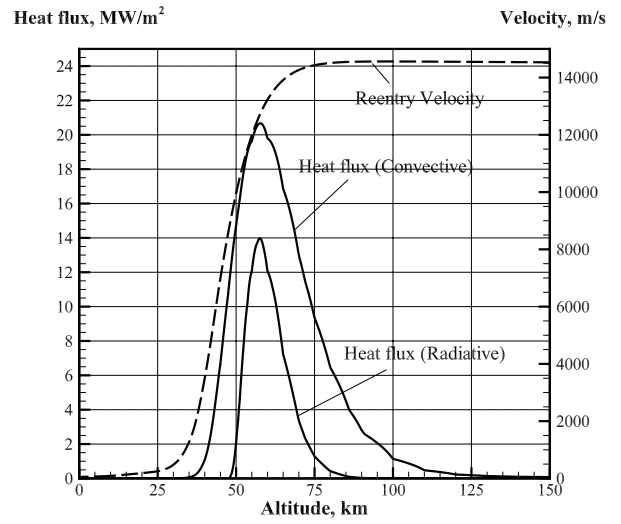
#### 3.2 Physical Models

The flow field is described by the Navier-Stokes equations with a multi-temperature model, which includes the translational, rotational, vibrational, and electron temperatures. The equations include total mass, momentum, total energy, species mass, vibrational energy, rotational energy, and electron energy conservation.

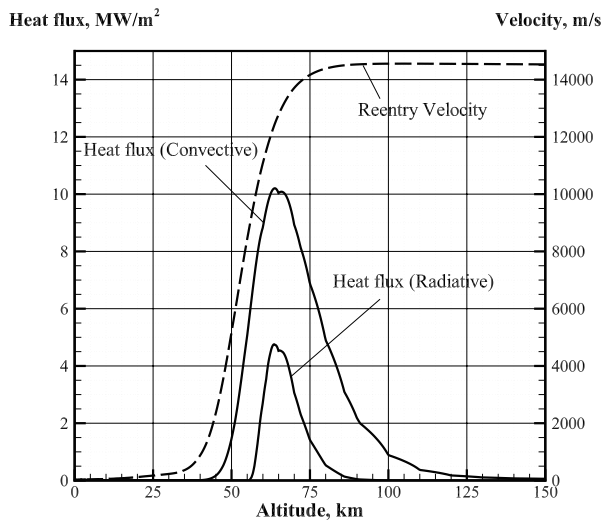
For chemical reactions in high-temperature air, the test gas is assumed to consist of 11 chemical species ( $N_2$ ,  $O_2$ ,  $NO$ ,  $N_2^+$ ,  $O_2^+$ ,  $NO^+$ ,  $N$ ,  $O$ ,  $N^+$ ,  $O^+$  and  $e^-$ ) and 49 reactions are assumed to occur. The chemical reaction rate is determined using an Arrhenius-type form; the



(a) Hayabusa SRC



(b) HVRC without rigid flare



(c) HVRC with rigid flare

Figure 3: Reentry trajectories and convective and radiative heat flux profiles calculated using empirical formulas.

forward reaction rate coefficients are obtained from Park’s work [11]. The backward reaction rate is calculated based on the corresponding equilibrium constants, which are obtained by the curve-fit formula according to Park’s work [12]. For the charge-exchange reaction between molecular and charged nitrogen ( $\text{N}_2 + \text{N}^+ \rightleftharpoons \text{N}_2^+ + \text{N}$ ), the parameters reported by Gupta et al. [13] were used.

The transport properties such as viscosity, thermal conductivity, and binary diffusion coefficients of the gas mixture are evaluated using Yos’ formula [14], which is based on the first Chapman-Enskog approximation [15]. The collision cross-sections are taken from a study by Gupta et al. [13]. However, for e-N and e-O pairs, the model by Fertig et al. [16, 17] is used. The diffusion coefficients are expressed using Curtiss and Hirschfelder’s formula [18]. Ambipolar diffusion is considered for charged species.

In the internal energy exchange model, the following energy transfers between each pair of internal energy modes are considered: translation-rotation (T-R) [19], translation-vibration (T-V) [20, 21], translation-electron (T-e) [22–24], rotation-vibration (R-V) [25], rotation-electron (R-e) [26, 27], and vibration-electron (V-e) [28, 29]. The energy losses or releases for vibrations and rotations associated with chemical reactions reveal the dissociation energies for heavy-particle-impact reactions. These are given by a non-preferential dissociation model [24]. The electron energy losses/releases due to electron-impact dissociation and ionization are also considered.

### 3.3 Numerical Procedure

The governing equations of the flow field are solved using a finite volume approach; the equation system is transformed into the delta form. All of the flow properties are set at the center of a control volume. The advection fluxes in the Navier-Stokes equations are calculated using the SLAU scheme [30] with the MUSCL interpolation to achieve high accuracy. On the other hand, the viscous fluxes are evaluated using the second-order central difference method. The solution to the system of equations is updated at each time step. Therefore, we employ the lower-upper symmetric Gauss-Seidel (LU-SGS) method coupled with the point-implicit method [31].

In the strong shock-wave region, the numerical instability of the rotational or the vibrational energy can occur because of a lack of molecules, which is caused by severe dissociation reactions when applying the proposed multi-temperature model. To overcome the stiffness, we introduce the switching model [32] of a two-temperature model, i.e., the heavy particle ( $T_{\text{trs}}=T_{\text{rot}}=T_{\text{vib}}$ .) and the electron temperatures  $T_{\text{ele}}$ , and we introduce a four-temperature model following a degree of mole fraction of molecular species. In the region where the molecular mole fraction is a small value,  $\varepsilon_{\text{mole}}$ , we adopt the two-temperature model instead of the four-temperature model. In this study, we set  $\varepsilon_{\text{mole}}$  to be  $10^{-3}$ .

### 3.4 Radiative Heat Flux

Considering a ray emitting a small element at a given position in a one-dimensional coordinate “ $s$ ”, the radiative transport equation in the system can be expressed as

$$\cos\theta \frac{dI_\lambda}{ds} = \kappa_\lambda (B_\lambda - I_\lambda), \quad (5)$$

where  $I_\lambda$ ,  $\kappa_\lambda$ , and  $B_\lambda$  represent the radiation intensity, absorption coefficient, and blackbody function at a given wavelength  $\lambda$ , respectively. In the proposed simulations, we adopt the

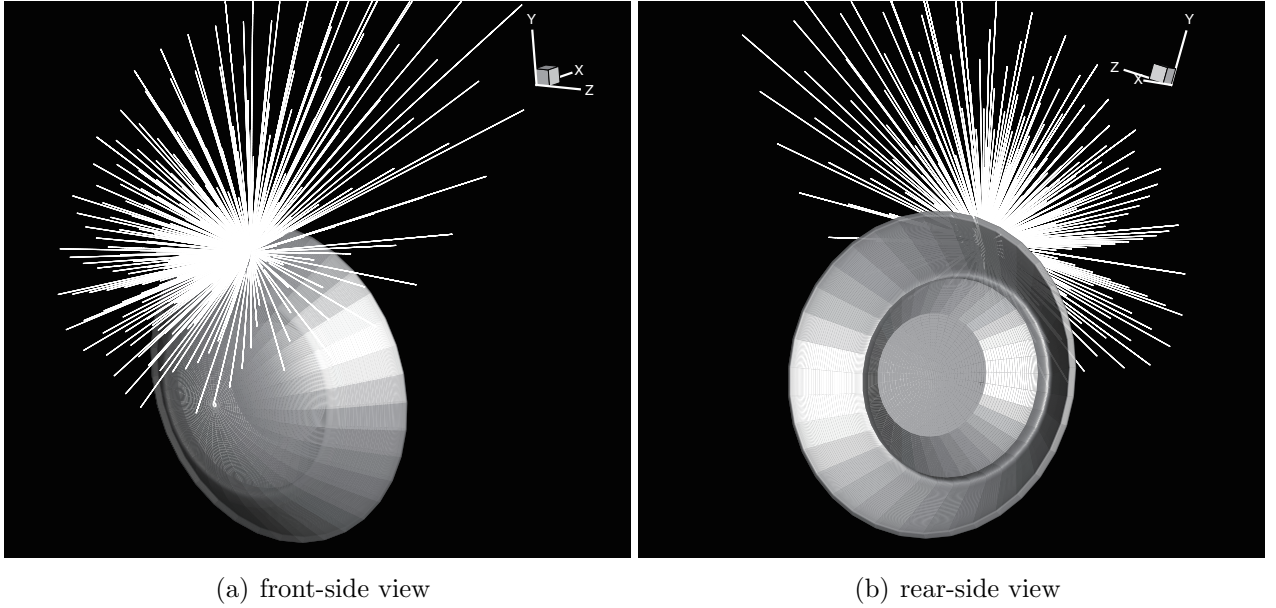


Figure 4: Example of ray distribution used to calculate radiative heat flux (HVRC with rigid flare).

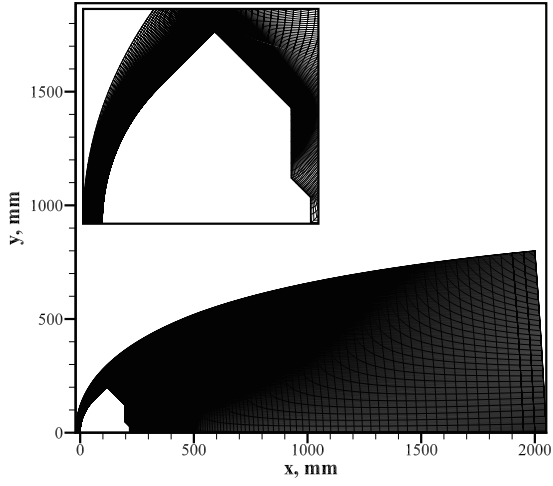
Boltzmann distribution to determine the population level of the electronic state. The absorption coefficient  $\kappa_\lambda$  includes the induced emission component.  $\theta$  is the angle between the ray and the coordinate  $s$ . The radiative heat flux to the element is calculated over the entire solid angle and all wavelengths, as follows:

$$q^{\text{rad}} = \iint I_\lambda \cos\theta d\Omega d\lambda. \quad (6)$$

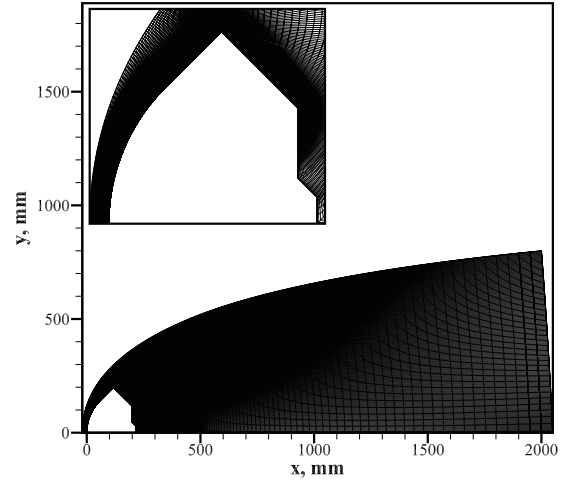
To calculate the radiative heat flux, 648 rays focusing on the surface of the reentry capsule emitted in all directions are defined as shown in Fig. 4. In the analysis case, the ray corresponds to a one-dimensional coordinate  $s$ , i.e.,  $\theta = 0$ . The radiative transport equation is integrated for all rays over spatial and wavelength regions. The absorption coefficients and blackbody function are obtained using the structured package for radiation analysis (SPRADIAN v1.5-PL4) [33] based on the flow field simulation results. In this calculation, radiation calculation is uncoupled with flow field simulation.

### 3.5 Computational Conditions

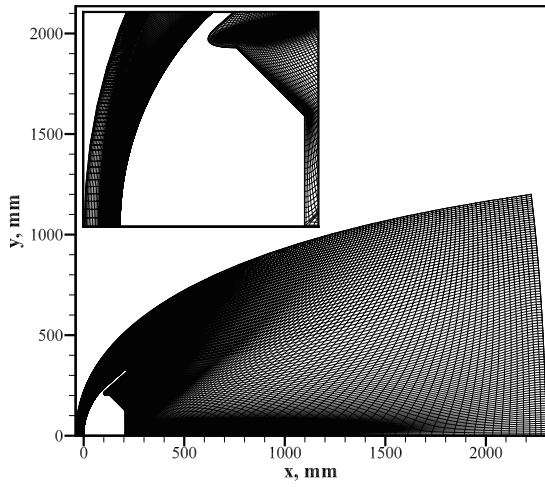
The computational grids for cases of 52.0 km, 57.9 km, and 64.0 km altitudes of Hayabusa SRC, the HVRC without rigid flare, and the HVRC with rigid flare are shown in Figs. 5(a), 5(b), and 5(c), although different grid systems are used at each altitude. We use structured grid systems for each analysis. The numbers of computational nodes in the grids are  $100 \times 202$  (axial  $\times$  radial) for Hayabusa SRC,  $150 \times 202$  for the HVRC without rigid flare, and  $100 \times 362$  for the HVRC with rigid flare, respectively. Aerodynamic heating for the case of the HVRC without a rigid flare is expected to be more severe than that for the case of the HVRC with a rigid flare because of the higher reentry velocity at the same altitude and atmospheric density. This is the reason for which the number of grid points in the axial direction of the HVRC without the rigid flare is set to be larger than that of the HVRC with the rigid flare.



(a) Hayabusa SRC at altitude of 52 km



(b) HVRC without rigid flare at altitude of 58 km



(c) HVRC with rigid flare at altitude of 64 km

Figure 5: Computational grids at altitude of peak aerodynamic heating.

For boundary conditions, at the inflow, the freestream parameters are given, following the trajectory data shown in Figs. 3(a), 3(b), and 3(c). At the outflow, all of the flow properties are determined by the zeroth order extrapolation. The non-slip condition for the velocity is imposed at the wall surfaces. The finite catalytic condition is expressed as follows:

$$D_i \frac{\partial C_i}{\partial n} = \gamma \sqrt{\frac{k N_A T_w}{2\pi M_i}} \rho_i, \quad (7)$$

where  $D_i$ ,  $C_i$ ,  $M_i$ , and  $n$  are the effective diffusion coefficient of species  $i$ , mass fraction, molar mass, and coordinate in the normal direction to the wall surface, respectively.  $k$  and  $N_A$  are the Boltzmann constant and the Avogadro constant, respectively. In this study, the catalytic coefficient  $\gamma$ , which is generally a value between 0 and 1, is set to 1. Thus, the fully catalytic condition for the mass concentration is imposed on the surface here. None of the pressure gradients is assumed to be normal to the wall. The translational, rotational, and vibrational temperatures are fixed at the wall and are set to 300 K as a cooling wall condition. The electron temperature is assumed to be adiabatic at the wall. An axisymmetric condition is imposed along the symmetry axis.

The present calculations for Hayabusa SRC, the HVRC without rigid flare, and the HVRC with rigid flare are performed for five cases that include altitudes at which peak aerodynamic heating occurs. The input parameters such as freestream velocity, density, and temperature are set according to the flight conditions as listed in Tables 2, 3, and 4. The degree of ionization at the inflow is always set to a small value,  $10^{-10}$ .

We perform a study of grid independencies using fine computational grids for Hayabusa SRC and HVRCs, as shown later. In the study, we show that the proposed computational grids are sufficiently convergent for heat-flux prediction.

## 4 Results and Discussion

### 4.1 Comparison of Surface Temperature

Hayabusa SRC had no on-board instruments to measure the high-enthalpy flow properties in the shock layer. On the other hand, on the ground, optical observation for the Hayabusa SRC fireball during atmospheric reentry was achieved by Fujita et al. [34]. The spectrum of grey-body radiation of the Hayabusa SRC surface using a charge-coupled device camera was observed. Then, the surface temperature was evaluated with the measured spectrum and numerical fitting with the blackbody radiation [2]. Because Hayabusa SRC was coated with an ablator heatshield on the surface, a thermal-response analysis of the ablator is required to predict the surface temperature. We conduct a one-dimensional analysis of the ablator heatshield of Hayabusa SRC. The analysis models, i.e., physical model and numerical model, are the same as those proposed by Potts [35]. The governing equations are the mass conservation of resin, momentum conservation of pyrolysis gas, and the energy conservation of pyrolysis gas and char. In this analysis, we consider the input convective and radiative heat fluxes for the cold-wall condition along the capsule-reentry trajectory, and we can obtain the temperature distribution, mass-flow rate of pyrolysis, and sublimation gases in the ablator. As mentioned above, we calculate these heat fluxes using the Detra-Kemp-Riddell [9] and Tauber-Sutton models [10]. We also obtain the thermochemical properties of the ablator according to Potts's work [35]. Figure 6 shows profiles of the surface temperature at an altitude, in addition to the convection and radiation heat fluxes. The figure also includes the surface

Table 2: Freestream condition of Hayabusa SRC.

Altitude, km	69.2	60.0	52.0	45.9	41.1
Density, kg/m <sup>3</sup>	$9.58 \times 10^{-5}$	$3.10 \times 10^{-4}$	$8.18 \times 10^{-4}$	$1.76 \times 10^{-3}$	$3.56 \times 10^{-3}$
Temperature, K	221.9	247.2	268.2	266.8	253.5
Velocity, m/s	11,554	11,029	9,799	7,949	5,571

Table 3: Freestream condition of HVRC without rigid flare.

Altitude, km	71.8	63.8	57.9	49.9	40.0
Density, kg/m <sup>3</sup>	$6.47 \times 10^{-6}$	$1.97 \times 10^{-4}$	$4.18 \times 10^{-4}$	$1.04 \times 10^{-3}$	$4.02 \times 10^{-3}$
Temperature, K	215.0	236.1	252.9	270.8	250.4
Velocity, m/s	14,337	13,790	12,783	9,897	3,482

Table 4: Freestream condition of HVRC with rigid flare.

Altitude, km	86.0	75.8	64.0	56.0	49.9
Density, kg/m <sup>3</sup>	$8.78 \times 10^{-6}$	$3.63 \times 10^{-5}$	$1.95 \times 10^{-4}$	$5.14 \times 10^{-4}$	$1.04 \times 10^{-3}$
Temperature, K	188.9	206.9	236.3	258.0	207.8
Velocity, m/s	14,500	14,213	12,496	9,052	5,114

temperature, which was measured using the ground-observation technique. The predicted surface temperature, which is based on the two heat-flux models, shows good agreement with the measured temperature. Thus, it is reasonable to use the heat-flux models to predict the aerodynamic heating at the stagnation point of Hayabusa SRC.

## 4.2 Hayabusa SRC

The CFD prediction model, which can correctly reproduce the aerodynamic heating environment around Hayabusa SRC [1, 2], may also be effective for the prediction of HVRCs with/without a rigid flare. The empirical models, the Detra-Kemp-Riddell and Tauber-Sutton models, which are used to evaluate the heat fluxes, are frequently used when designing reentry capsules. These empirical models were the design tools used to create Hayabusa SRC, and they show reasonable performance in the prediction of aerodynamic heating at stagnation. Therefore, as mentioned above, we expect that a comparison of the CFD approach with the empirical models should be one of the benchmarks that indicate whether the solution obtained by CFD is reasonable, although the comparison may be indirect.

Figure 7 shows a comparison of convective and radiative heat fluxes at the stagnation point of Hayabusa SRC between the empirical models and the present CFD model. The convective and radiative heat fluxes predicted using the CFD approach are in good agreement with those obtained using the empirical models. In particular, the CFD approach can accurately reproduce heat fluxes at low altitude, where the air density is high and the flow field is close to the thermochemical equilibrium state. On the other hand, the results indicate that the radiative heat flux by the CFD is slightly overestimated at high altitude, where the air

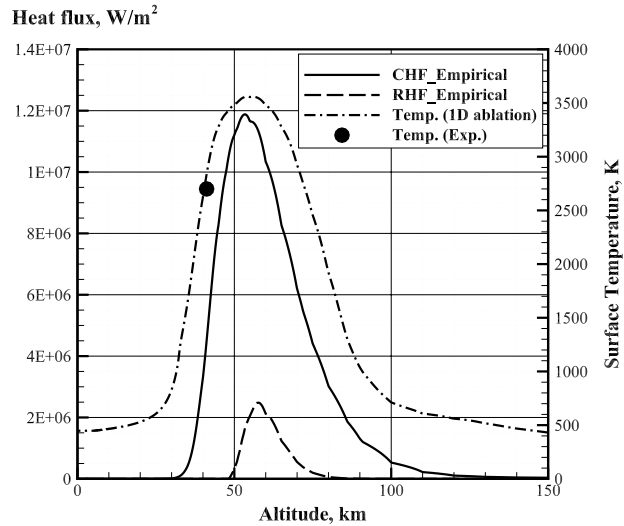


Figure 6: Comparison of surface temperature, convective and radiative heat fluxes at stagnation point of Hayabusa.

density is low. This can be attributed to uncertainty in the thermochemical nonequilibrium models, such as internal energy exchange models and chemical reaction models.

The distribution of the convective and radiative heat fluxes along the surface of Hayabusa SRC at an altitude of 52.0 km is shown in Fig. 8. At the front heat shield, the convective and radiative heat fluxes are 12.3 MW/m<sup>2</sup> and 1.0 MW/m<sup>2</sup>, respectively. Convection is dominant at this altitude. On the other hand, at the rear of the capsule, the convective and radiative heat fluxes are 0.16 MW/m<sup>2</sup> and 0.4 kW/m<sup>2</sup>, respectively. The total heat flux at the rear is less than 2% of that at the front. It was implied that the heat shield at the rear might not have been exposed to strong aerodynamic heating during the actual reentry phase; the result in this analysis shows that this conclusion is reasonable based on the tendency obtained for Hayabusa SRC flight. However, because ablation injection during actual reentry of Hayabusa SRC occurred [36], we believe that enhancement of radiation by ablation gas in the shock layer and wake region occurred. Because the heat flux distribution on the surface under the cooling wall condition is an important design parameter, ablation analysis is not treated in the present model. There are several uncertainties that inhibit the development of physical and numerical models related to ablation. In addition, the numerical cost tends to become large because of the increase in the number of chemical species (and therefore, the chemical reactions) that must be considered. Therefore, analyzing the ablation gas in the flow field remains an object of future study, although we require an analysis coupled with the flow field when predicting the aerodynamic heating more accurately.

### 4.3 HVRC without Rigid Flare

As described in the comparison of the trajectory data (Fig. 3), aerodynamic heating around the HVRC without a rigid flare is the strongest of the three cases considered here; this is caused by its ballistic coefficient and reentry velocity. Figure 9 shows heat fluxes of convection and radiation at the stagnation point of the HVRC without a rigid flare for both the empirical models and the CFD approach. The convective heat fluxes computed using CFD are similar

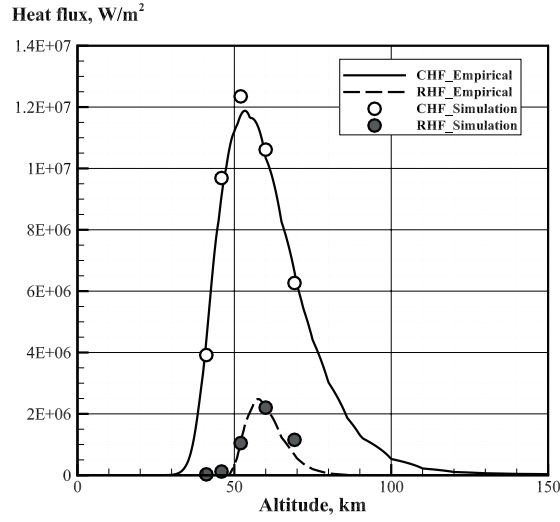


Figure 7: Comparison of convective and radiative heat fluxes at stagnation point of Hayabusa SRC between empirical formula and CFD approach.

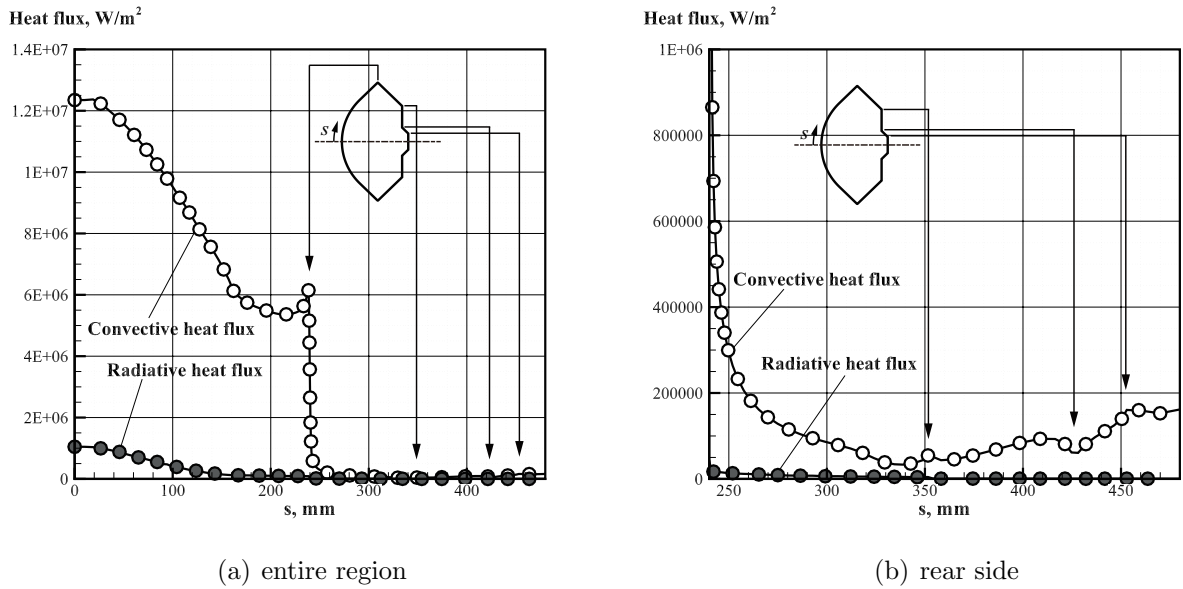


Figure 8: Distribution of convective and radiative heat fluxes along the surface of Hayabusa SRC at an altitude of 52.0 km.

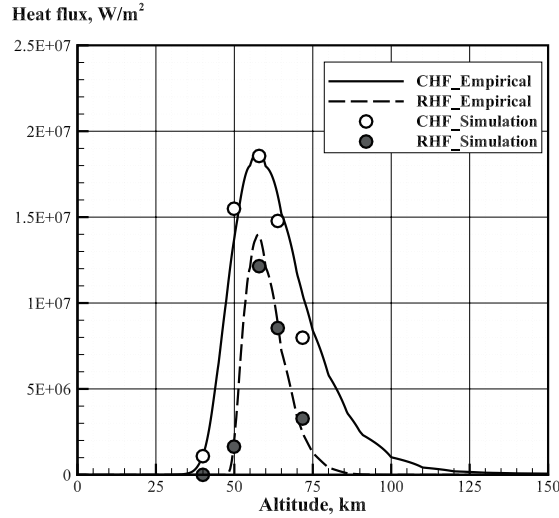


Figure 9: Comparison of convective and radiative heat fluxes at stagnation point of HVRC without a rigid flare between empirical formula and CFD approach.

to those computed using the empirical model at low altitudes, whereas there appear to be discrepancies at high altitudes. Radiative heat flux calculated using CFD underestimates that by the empirical model, although predictions made using CFD and empirical approaches agree well at other altitudes.

Convective and radiative heat flux distributions along the surface of the HVRC without a rigid flare at an altitude of 57.9 km are shown in Fig. 10. At the front of the capsule, the convective and radiative heat fluxes are approximately 18.6 MW/m<sup>2</sup> and 12.1 MW/m<sup>2</sup>, respectively. Both convection and radiation are significant at this altitude. At the shoulder part of the capsule ( $s = 240\text{-}340$  mm), radiation and convection components become nearly equal. This feature near the shoulder does not appear in the analysis of Hayabusa SRC and the HVRC with a rigid flare, as described below. On the other hand, at the rear heat shield, the convective and radiative heat fluxes are 0.48 MW/m<sup>2</sup> and 6.0 kW/m<sup>2</sup>, respectively. The radiation's contribution to the heat flux at the rear side significantly decreases. The total heat flux at the rear is less than 2% of that at the front. The distributions of convective heat flux of the HVRC without a rigid flare are similar to those of the Hayabusa SRC; significant enhancement of radiation is a feature in the aerodynamic heating environment around the capsule.

The axial profiles of the temperatures and the mole fractions along the center axis of the HVRC without a rigid flare at an altitude of 57.9 km are shown in Figs. 11(a) and 11(b), respectively. In the shock wave, temperatures are completely separated into the translational, rotational, vibrational, and electron modes, and a strong nonequilibrium region appears. In particular, the translational temperature reaches approximately 70,000 K due to the very high velocity. The electron temperature increases upstream of the shock wave. This is mainly because the thermal conductivity of the electrons becomes relatively high in the region of the low electron density, and there is heat conduction from the shock layer. The rotational and vibrational temperatures increase because of relaxations with the translational energy mode in the shock wave. Molecules are almost dissociated, and we adopt a two-temperature model following the switching model of the multi-temperature model. In the region where

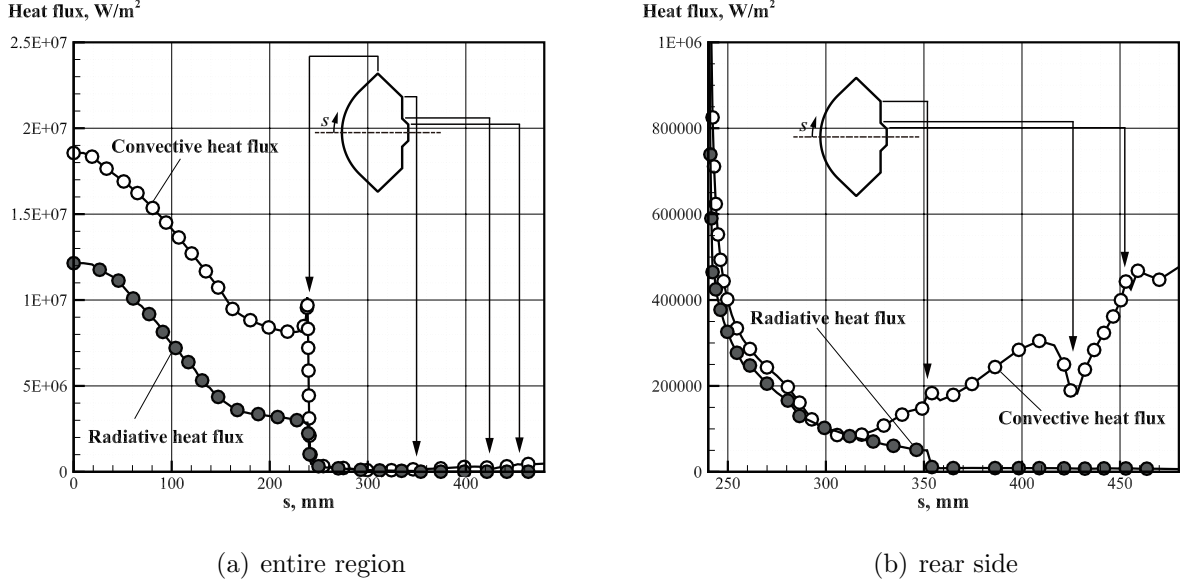
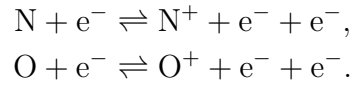


Figure 10: Distribution of convective and radiative heat fluxes along the surface of HVRC without a rigid flare at an altitude of 57.9 km.

the number of molecules becomes low ( $x \geq -9$  mm), rotational and vibrational energies that are proportional to the molecule densities also become low, and then, these energy modes have a small impact on the flow field. Rapid dissociation reactions of the molecular nitrogen and the molecular oxygen occur across the shock wave. On the other hand, the equilibrium region is the region in which the temperature is also equilibrated behind the shock wave. In the equilibrium region, ionized gas such as charged atomic nitrogen and electrons, and atomic nitrogen are dominant. Because of the high reentry velocity, even at low altitudes, a large number of electrons is generated in front of the HVRC without a rigid flare. Thus, radiation is generally enhanced at all altitudes. This tendency for the radiation effect to become stronger can be reproduced by the CFD in a similar fashion to that when using the empirical model. Because the electron temperature reaches approximately 13,300 K in the equilibrium region of the high-density shock layer for the case of the HVRC without a rigid flare, dominant ionization reactions become electron-impact ionizations in the CFD approach, as follows:



The electron-impact ionization continuously creates electrons via the avalanche process. Thus, radiation, which is strongly affected by electron temperature and electron density, can be rapidly enhanced when exceeding a certain threshold of reentry velocity and density of air. Note that the electron-impact ionizations prominently occur at an altitude of 71.8 km in the CFD results. Figures 12(a) and 12(b) show distributions of the electron temperature and the density of electrons, respectively, around the HVRC without a rigid flare at an altitude of 57.9 km. The electron-number density in Fig. 12(b) is represented with a logarithmic scale. The distribution of the gradient-length local Knudsen number [37] around the HVRC without a rigid flare at an altitude of 57.9 km (Fig. 13) is defined by

$$Kn_{\text{GLL}} = \max \{ Kn_{\text{GLL}}(\rho), Kn_{\text{GLL}}(u), Kn_{\text{GLL}}(T_{\text{trs}}) \}.$$

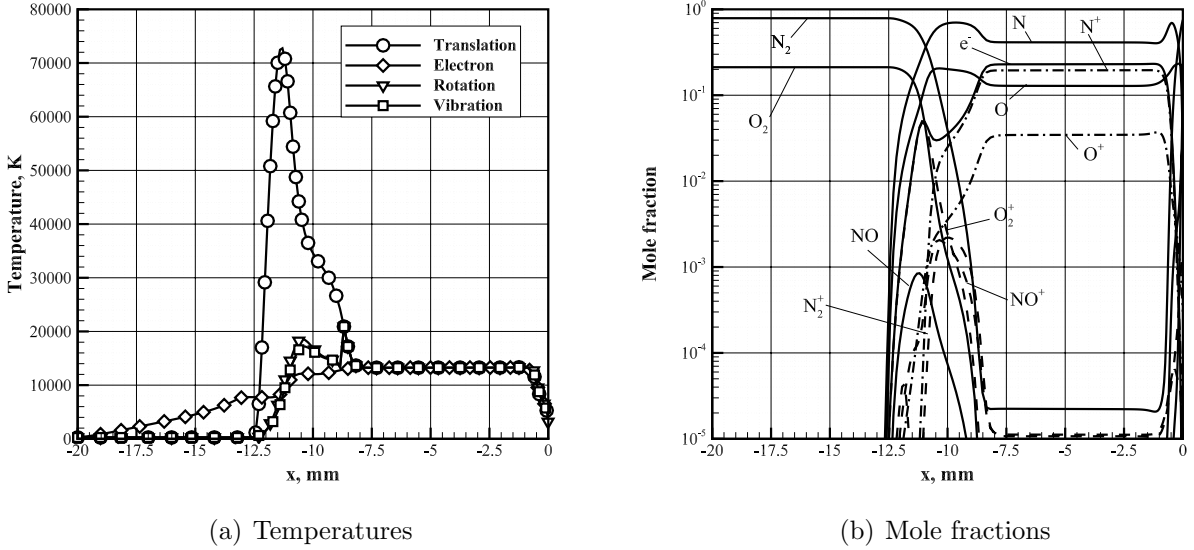


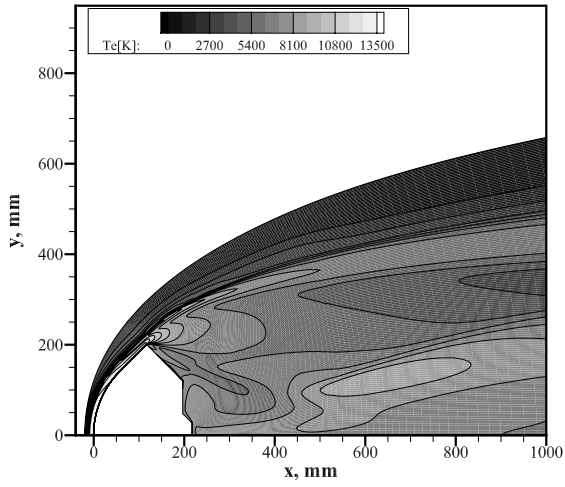
Figure 11: Axial profiles of plasma-flow properties along center axis of the HVRC without a rigid flare at an altitude of 57.9 km.

Using the mean free path  $\lambda$ , the equation can be rewritten as

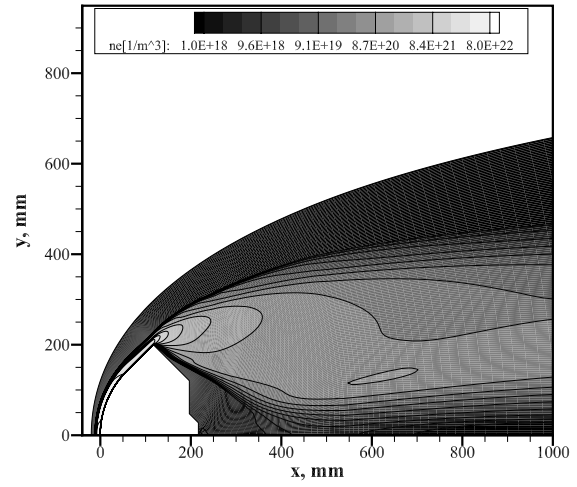
$$Kn_{\text{GLL}}(Q) = \frac{\lambda}{Q} \left| \frac{\partial Q}{\partial x} \right|.$$

The maximum value in the legend of the figure ( $Kn_{\text{GLL}} = 0.05$ ) shows a typical continuum breakdown value. The local Knudsen number along the shock wave in front of the reentry capsule is high. When plasma flows into the wake region from the shoulder part of the capsule, the compressed gas is rarefied and cooled behind the aft of the capsule. However, the local Knudsen number in the region is of the order of  $10^{-3}$  except for these limited regions. Therefore, the continuum assumption is expected to be sufficiently justified. Although the flow is in supersonic expansion in the wake, electrons are recombined at a slow rate and a large number of electrons remains near the capsule surface behind the shoulder. Thus, radiation does not rapidly become weak near the shoulder, unlike in the case of Hayabusa SRC. These are the primary reasons why the radiative heat flux is high at the front and shoulder parts for the HVRC without a rigid flare.

In this study, we use the Boltzmann distribution to determine the population of electronic states. On the other hand, it has been reported by Johnston et al. [8,38] that nonequilibrium-level population can change the radiative heat flux around the reentry capsule. In particular, the radiative heat flux at the rear of the capsules considering the non-Boltzmann distribution is higher than that considering the Boltzmann distribution. For a more accurate prediction of the heating environment and a safe-side estimation of heat flux for a capsule, it is desirable to consider the non-Boltzmann distribution in high-temperature gas simulations. However, it is necessary to introduce various complicated models, and numerical operation incurs a large computational cost. This issue may be the focus of future works.



(a) electron temperature



(b) number density of electrons

Figure 12: Distribution of electron properties around the HVRC without a rigid flare at an altitude of 57.9 km.

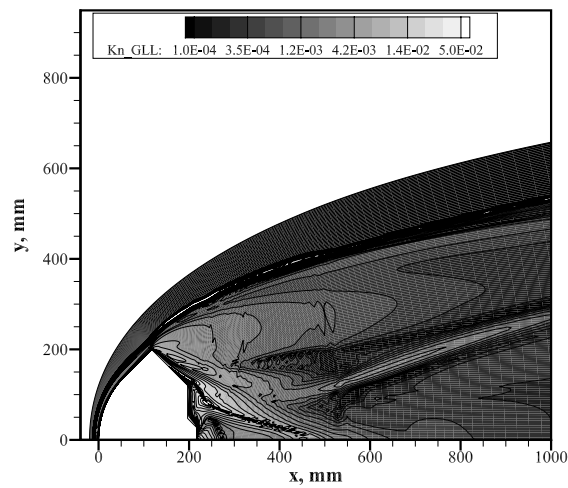


Figure 13: Distribution of gradient-length local Knudsen number around the HVRC without a rigid flare at an altitude of 57.9 km.

## 4.4 HVRC with Rigid Flare

A comparison of heat fluxes at the stagnation point of the HVRC with a rigid flare between the empirical models and CFD is shown in Fig. 14. Similar to the results for Hayabusa SRC, the results computed using the CFD approach reproduce those of the empirical models, except in the case of an altitude of 75.8 km. However, it should be noted that there appear to be slight discrepancies between the two methods; the convective heat flux at a high altitude and radiative heat flux at all altitudes via CFD tend to overestimate those via empirical models. From the results of the HVRC with a rigid flare in addition to Hayabusa SRC and the HVRC without a rigid flare, it is indicated that the present CFD and the empirical models have different performance when predicting aerodynamic heating at a higher altitude, where a nonequilibrium flow field becomes dominant. At present, it is difficult to validate the physical models used here in a high-velocity, low-density environment. To solve this problem, uncertainty analysis of the physical models can become an effective method. Moreover, in the present calculation, radiative heat flux is calculated based on the converged solutions from a flow-field solver, whereas the two-way coupling calculation of radiation with flow-field analysis is not performed. According to Fujita's work [2] for Hayabusa SRC, the coupling calculation between radiation and flow-field reduced heat flux on the surface of the capsule. To allow more accurate prediction, the introduction of radiation coupling may be required.

Tendencies of convective and radiative heat fluxes between the CFD approach and the empirical models are significantly different at an altitude of 75.8 km. Strong electron-impact ionization reactions occur in the present CFD approach at this altitude, whereas the reactions occur less often in the CFD result at an altitude of 86.0 km. Because a large number of electrons is generated by the reactions, radiative heat flux increases. On the other hand, because the temperature gradient in the shock layer decreases (because of transfer from thermal energy to chemical energy by the reactions), the convective heat flux decreases. At an altitude of 86.0 km, the computed result of the convective heat flux overestimates the empirical result. The Detra-Kemp-Riddell method that is used herein was constructed based on the continuum flow assumption. In Eq. (2), which is an expression of the Detra-Kemp-Riddell method, no thermochemically nonequilibrium is considered. We believe that the difference between the results obtained by the CFD technique and the empirical methods is due to the thermochemical nonequilibrium models. Note that the global Knudsen number using the diameter of 0.66 m as the characteristic length is of the order of  $10^{-2}$  for the case at an altitude of 86.0 km, and the flow field is confirmed to be sufficiently continuum.

Figure 15 shows the distribution of the convective and radiative heat fluxes along the surface of the HVRC with a rigid flare at an altitude of 64.0 km, at which aerodynamic heating reaches its peak value during reentry. The heat flux profile at the front of the capsule is similar to that of Hayabusa SRC. At the front of the HVRC with a rigid flare, convective and radiative heat fluxes are  $9.2 \text{ MW/m}^2$  and  $5.3 \text{ MW/m}^2$ , respectively. On the other hand, at the rear, the convective and radiative heat fluxes are  $0.26 \text{ MW/m}^2$  and  $10 \text{ kW/m}^2$ , respectively. Although the ratio of radiation to total heat flux is large compared the the result of Hayabusa SRC, the total heat flux at the rear is approximately 2% of that at the front, which is similar to the HVRC without a rigid flare.

Although air density is low at an altitude of 64.0 km, an equilibrium region appears in the shock layer because of the high reentry velocity; gas temperature in the region is approximately 12,500 K at this altitude. In addition, dissociation and ionization reactions rapidly proceed in the shock layer. Figures 16(a) and 16(b) show the axial profiles of temperatures and mole fractions along the center axis of the HVRC with a rigid flare at an altitude of 64.0

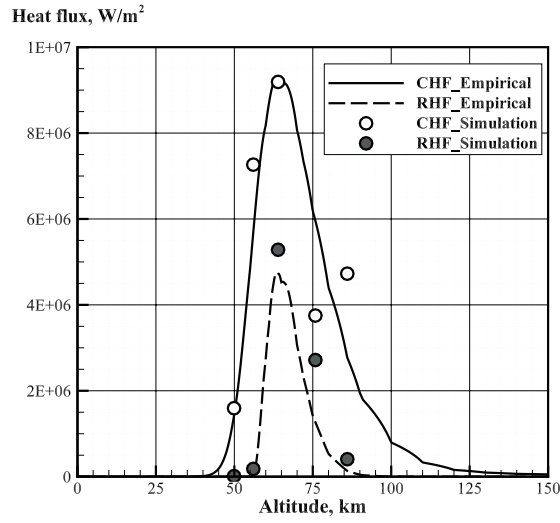


Figure 14: Comparison of convective and radiative heat fluxes at stagnation point of HVRC with a rigid flare between empirical formula and CFD approach.

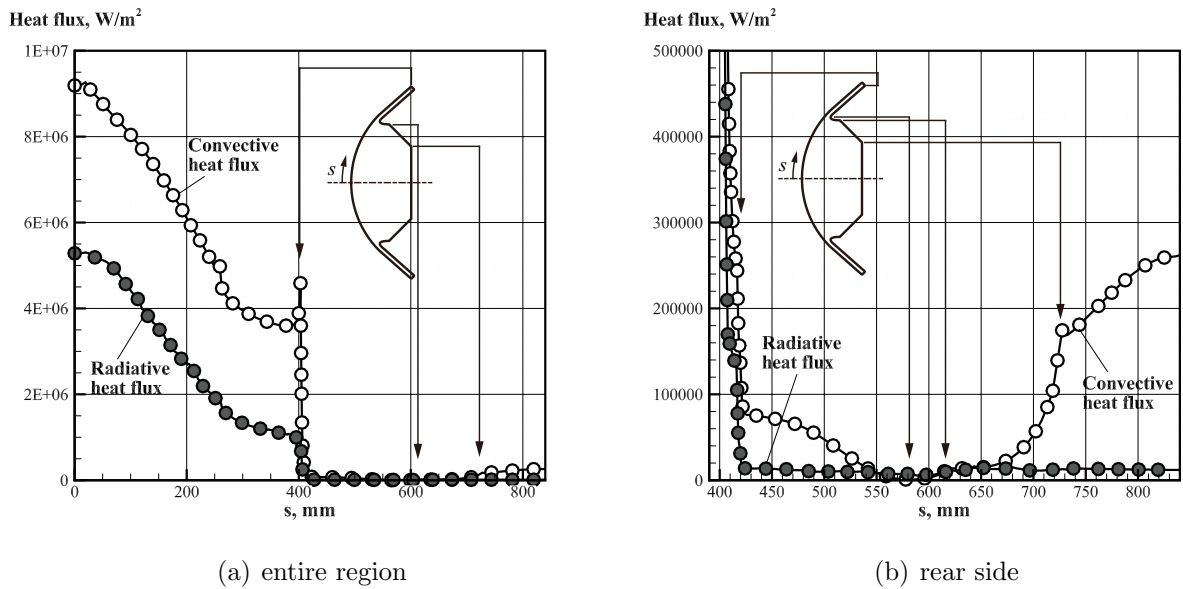


Figure 15: Distribution of convective and radiative heat fluxes along the surface of HVRC with a rigid flare at an altitude of 64.0 km.

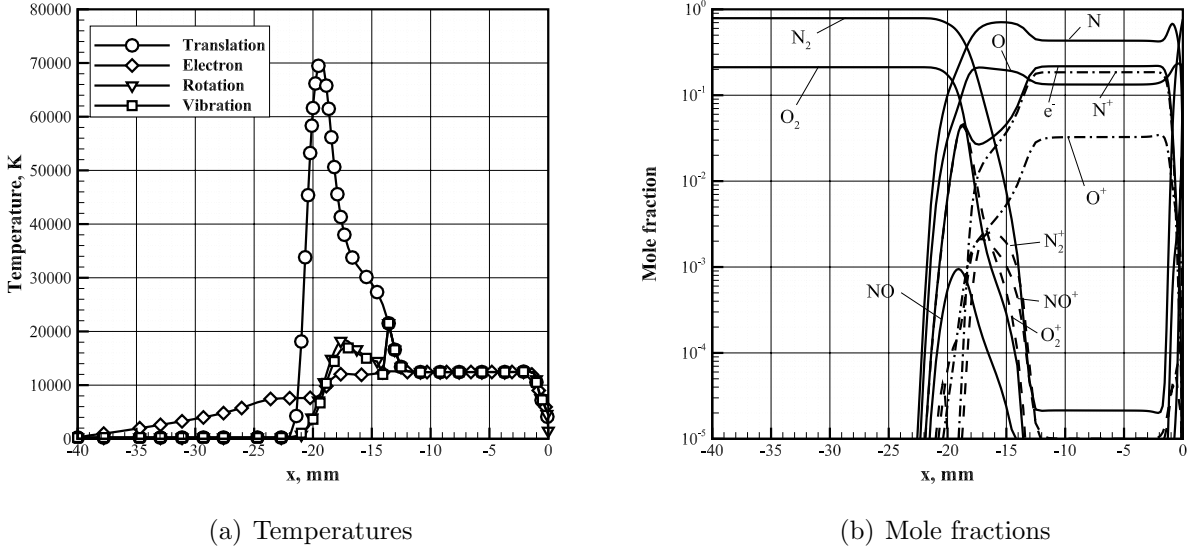


Figure 16: Axial profiles of plasma-flow properties along center axis of the HVRC with a rigid flare at an altitude of 64.0 km.

km. Trends of the temperatures and mole fractions are very similar to those obtained for the case of the HVRC without a rigid flare, although the thickness of the shock layer increases because of the low freestream density at a higher altitude. A strong nonequilibrium appears across the shock wave, while an equilibrium region is created in the shock layer. The mole fraction of electrons is approximately 0.22 in the equilibrium region at an altitude of 64.0 km; this is mainly caused by electron-impact dissociation and ionization reactions. High electron temperatures and a high degree of ionization enhance radiation intensity for the HVRC with a rigid flare. D'Angola et al [39] reported that the first Chapman-Enskog approximation (used in this study) has increased errors in the high temperature region (defined as gas temperatures of over 10,000 K). Thus, more accurate transport models, such as a higher order Chapman-Enskog models, remain to be introduced in future work.

Figures 17(a) and 17(b) show the distributions of electron temperature and number density of electrons around the HVRC at an altitude of 64.0 km, respectively. Note that the electron number density is represented in a logarithmic scale. The electron temperature is 12,500 K in the shock layer, and then, decreases to approximately 8,000 K throughout the wake region. The number density of electrons is also kept high in the wake, because insufficient recombination reactions between electrons and heavy particles occurs. On the other hand, at the aft of the capsule, the electron density is rarefied because of expansion when inflowing at the rear. Figure 18 shows the distribution of the gradient-length local Knudsen number around the HVRC with a rigid flare at an altitude of 64.0 km. Similar to an HVRC without a rigid flare, the local Knudsen number in the limited regions near the shock wave and in the wake region partly exceeds the breakdown parameter, whereas the local Knudsen number around the capsule except for these regions is of the order of  $10^{-2}$ . It is shown that this rarefied gas region is slightly larger than that of the HVRC without a rigid flare (see also Fig. 13). Because radiation intensity strongly depends on electron temperature and electron number density, radiation emitted from the aft gas decreases, which is the reason the radiative heat flux is low at the rear of the capsule (as discussed above). This reduction of aerodynamic heating at the rear is expected to become an advantage for capsules with a

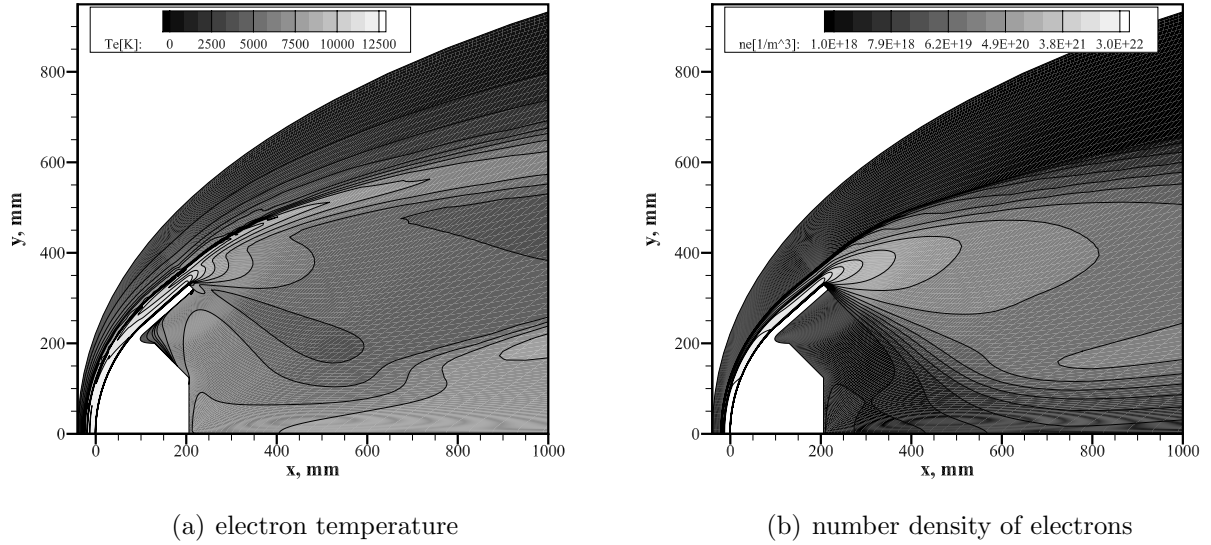


Figure 17: Distributions of electron properties around the HVRC with a rigid flare at an altitude of 64.0 km.

large projected flare area.

When the flow field around the reentry capsule is fully turbulent, unsteady flow and a three-dimensional structure can appear in the rear region, and they can drastically change the aerodynamic hearing situation on the aft surface. However, because the Reynolds numbers of the three reentry capsules are approximately  $10^5$  at peak aerodynamic heating altitudes, the flow fields are expected to be laminar or partly turbulent. In fact, a fully turbulent flow may appear at lower altitudes, while the turbulence does not affect the aerodynamic heating, but the aerodynamic characteristics, because the reentry capsules are sufficiently decelerated. We considered that the assumption of the axisymmetric two dimension and the steady flow used in this study are justified for the prediction of aerodynamic heating.

## 4.5 Grid Study

To investigate the independency of the computational grids used in this study, we perform grid studies at altitudes of 52.0 km for Hayabusa SRC, 57.9 km for the HVRC without the rigid flare, and 64.0 km for the HVRC with the rigid flare. We use fine computational grids with node numbers of  $200 \times 356$  for Hayabusa SRC,  $250 \times 395$  for the HVRC without the rigid flare, and  $200 \times 703$  for the HVRC with the rigid flare, respectively. Comparisons of convective heat fluxes at the stagnation point of Hayabusa SRC, the HVRC without the rigid flare, and the HVRC with the rigid flare, are shown in Table 5, 6, 7, respectively. Errors in the heat fluxes for cases using the present and fine grids are within the range of several percentages. Figures 19(a) and 19(b) show comparisons of temperatures along the stagnation line of HVRCs for cases using the present and fine grids. The temperatures profiles for the present and fine grids cases are closely agree. Although figure for Hayabusa SRC is not shown here, it is confirmed that differences between temperatures profile for the present and fine grids is not almost appear. Considering that temperature distribution in the equilibrium region has large impact on the radiation intensity, this result of comparisons indicate that radiative heat fluxes for reentry capsules are also sufficiently convergent.

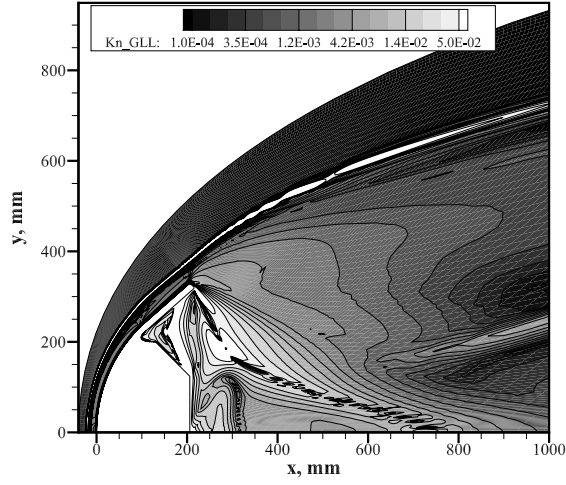


Figure 18: Distribution of gradient-length local Knudsen number around the HVRC with a rigid flare at an altitude of 64.0 km.

Table 5: Grid sensitivity for Hayabusa SRC between present and fine grids.

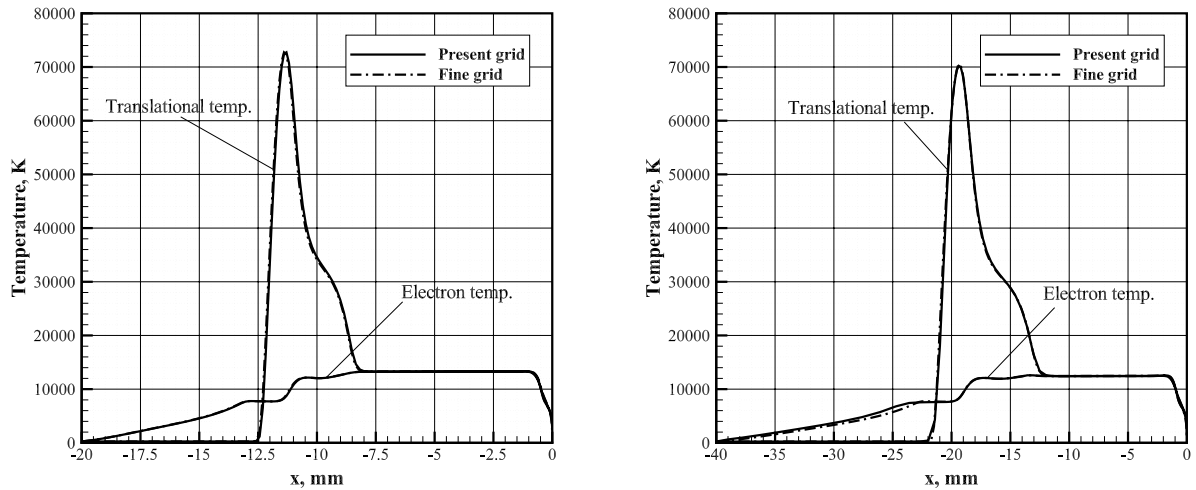
	Present	Fine	Error, %
Number of grids	$100 \times 202$	$200 \times 356$	–
Heat flux, $\text{W/m}^2$	$1.23 \times 10^7$	$1.28 \times 10^7$	3.68

Table 6: Grid sensitivity for HVRC without the rigid flare between present and fine grids.

	Present	Fine	Error, %
Number of grids	$150 \times 202$	$250 \times 395$	–
Heat flux, $\text{W/m}^2$	$1.86 \times 10^7$	$1.98 \times 10^7$	6.34

Table 7: Grid sensitivity for HVRC with the rigid flare between present and fine grids.

	Present	Fine	Error, %
Number of grids	$100 \times 362$	$200 \times 703$	–
Heat flux, $\text{W/m}^2$	$9.19 \times 10^6$	$9.42 \times 10^6$	2.41



(a) HVRC without the rigid flare at an altitude of 58 km (b) HVRC with the rigid flare at an altitude of 64 km

Figure 19: Comparison of translational and electron temperatures for HVRCs using present and fine grids as grid sensitivity.

## 4.6 Aft Shell Heating

In the design and development of the Hayabusa SRC, the heat flux at the aft of the capsule was set to be 10 % of that at the stagnation point. An excess margin for the heat resistance against aerodynamic heating was possibly ensured. In the present study, it is indicated that heat fluxes at the aft of the HVRCs and the Hayabusa SRC are approximately 2 % of that at the stagnation points. These findings are effective in reducing the weight of the heat shield at the back shell ablator of the reentry capsules. On the other hand, however, we should admit that the present analysis model does not indicate the reasonability of the heat flux prediction at the capsule rears with model validation because it is very difficult to reproduce an aerodynamic heating environment generated by a high-velocity flow of 15 km/s using ground-based wind tunnels. In addition, there is almost no data available for comparison and validation of the analysis model. Needless to say, these are the important issues in addition to the formulation and validation of ablator and radiation models.

## 5 Conclusions

Two HVRCs were proposed based on the actual properties of Hayabusa SRC. One of the HVRCs was designed to achieve low ballistic coefficient flight with an attached rigid flare on the capsule edge. The other HVRC was designed to use the configuration of Hayabusa SRC without changes based on aerodynamic data obtained during the Hayabusa mission. The maximum reentry velocities of Hayabusa SRC and the HVRCs were 12 km/s and 15 km/s, respectively. Analyses of aerodynamic heatings for Hayabusa SRC and high HVRC without/with a rigid flare were performed for several altitudes using a CFD approach. Both the convective and radiative heat fluxes for Hayabusa SRC and the HVRC without/with a rigid flare via the CFD approach were in good agreement with results from empirical models used in the phases of design and development of the reentry capsule. However, it was

clarified that the tendencies of heat flux profiles between the CFD and the empirical models are different at the altitude at which the electron-impact ionizations strongly occur. For both of the HVRCs, it was indicated that the ratio of convective heat flux to radiative heat flux was on the same order as at its front heat shield side, whereas radiation decreased at the rear region. At the peak aerodynamic heating altitude, the total heat flux of the HVRC's rear heat shield was approximately 2% of that at the front. However, there were large differences in aerodynamic heating between the HVRC with and that without a rigid flare, because of the ballistic coefficients.

The present analysis model was constructed based on the concept of predicting the heat flux for a cooled temperature wall condition at the initial stage of design and development of reentry capsule. Thus, ablator gas analysis and radiation coupling with flow field simulation were not introduced. For a more accurate prediction of aerodynamic heating, it is essential to include related models in the present analysis model. In addition, the reentry velocity of the HVRC is significantly higher than that of the Hayabusa SRC. An increase in the reliability of the analysis model is required; this can be achieved through comparison and validation with experiments, e.g., in an expansion tube or an arc-heated wind tunnel.

## Acknowledgments

The authors of the paper would like to thank Mr. Tamon Nakano, École Nationale Supérieure de Mécanique et d'Aéronautique de Poitiers (ENSMA), for his valuable cooperation. The computations were carried out using the computational facilities (HITACHI HA8000-tc/HT210) at the Research Institute for Information Technology, Kyushu University, and the supercomputer system (HITACHI SR16000 model M1) at the Information Initiative Center, Hokkaido University.

## References

- [1] H. Otsu, K. Suzuki, K. Fujita, and T. Abe. "Assessment of Forebody and Backbody Radiative Heating Rate of Hypervelocity Reentry Capsule". ISAS Report SP 17, Institute of Space and Aeronautics Science, Sagamihara, Japan, March 2003.
- [2] K. Fujita, T. Suzuki, S. Matsuyama, T. Yamada, and S. Abe. "Numerical Reconstruction of HAYABUSA Sample Return Capsule Flight Environment". *AIAA Paper 2011-3477*, 2011.
- [3] D. Olynick, Y.K. Chen, and M.E. Tauber. "Aerothermodynamics of the Stardust Sample Return Capsule". *Journal of Spacecraft and Rockets*, 36(3):442–462, May-June 1999.
- [4] R.N. Gupta. "Aerothermodynamic Analysis of Stardust Sample Return Capsule with Coupled Radiation and Ablation". *Journal of Spacecraft and Rockets*, 37(4):507–514, July-August 2000.
- [5] R. Funase, O. Mori, Y. Shirasawa, and H. Yano. "Trajectory Design and System Feasibility Analysis for Jovian Trojan Asteroid Exploration Mission Using Solar Power Sail". *Transactions of the Japan Society for Aeronautical and Space Sciences, Aerospace Technology Japan*, 12(ists29):Pd.85–Pd.90, 2014.

- [6] J. Matsumoto, R. Funase, O. Mori, Y. Shirasawa, G. Ono, T. Hamasaki, N. Hayashi, T. Chujo, N. Motooka, and K. Tanaka. “Mission Analysis of Sample Return from Jovian Trojan Asteroid by Solar Power Sail”. *Transactions of the Japan Society for Aeronautical and Space Sciences, Aerospace Technology Japan*, 12(ists29):Pk.43–Pk.50, 2014.
- [7] P. Tsou, D.E. Brownlee, C.P. McKay, A.D. Anbar, H. Yano, K. Altwegg, L.W. Beegle, R. Dissly, N.J. Strange, and I. Kanik. “LIFE: Life Investigation for Enceladus A sample Return Mission Concept in Search for Evidence of Life”. *Astrobiology*, 12(8):730–742, 2012.
- [8] C.O. Johnston, J. Samareh, and A.M. Brandis. “Aerothermodynamic Characteristics of 16 – 22 km/s Earth Entry”. *AIAA Paper 2015-3110*, 2015.
- [9] R.W. Detra, N.H. Kemp, and F.R. Riddell. “Addendum to Heat Transfer to Satellite Vehicles Re-entering the Atmosphere”. *Jet Propulsion*, 27(12):1256–1257, December 1957.
- [10] M.E. Tauber and K. Sutton. “Stagnation-Point Radiative Heating Relation for Earth and Mars Entries”. *Journal of Spacecraft and Rockets*, 28(1):40–42, September-October 1991.
- [11] C. Park. “Assessment of a Two-Temperature Kinetic Model for Dissociating and Weakly Ionizing Nitrogen”. *Journal of Thermophysics and Heat Transfer*, 2(1):8–16, Jan.-March 1988.
- [12] C. Park. *Nonequilibrium Hypersonic Aerothermodynamics*. Wiley, New York, 1990.
- [13] R.N. Gupta, J.M. Yos, R.A. Thompson, and K.P. Lee. “A Review of Reaction Rates and Thermodynamic and Transport Properties for an 11-Species Air Model for Chemical and Thermal Nonequilibrium Calculations to 30000 K”. *NASA RP-1232*, Aug. 1990.
- [14] J.M. Yos. “Transport Properties of Nitrogen, Hydrogen Oxygen and Air to 30,000 K”. *TRAD-TM-63-7*, Research and Advanced Development Division, AVCO Corp., 1963.
- [15] J.O. Hirschfelder, C.F. Curtiss, and R.B. Bird. *Molecular Theory of Gases and Liquids*. Wiley, New York, 1954.
- [16] M. Fertig, A. Dohr, and H.H. Frühauf. “Transport Coefficients for High-Temperature Nonequilibrium Air Flows”. *AIAA Paper 98-2937*, 1998.
- [17] M. Fertig, A. Dohr, and H.H. Frühauf. “Transport Coefficients for High-Temperature Nonequilibrium Air Flows”. *Journal of Thermophysics and Heat Transfer*, 15(2):148–156, April-June 2001.
- [18] C.F. Curtiss and J.O. Hirschfelder. “Transport Properties of Multicomponent Gas Mixture”. *Journal of Chemical Physics*, 17(6):550–555, June 1949.
- [19] J.G. Parker. “Rotational and Vibrational Relaxation in Diatomic Gases”. *The Physics of Fluids*, 2(4):449–462, July-Aug. 1959.
- [20] R.C. Millikan and D.R. White. “Systematics of Vibrational Relaxation”. *The Journal of Chemical Physics*, 39(12):3209–3213, Dec. 1963.

- [21] C. Park. “Problems of Rate Chemistry in the Flight Regimes of Aeroassisted Orbital Transfer Vehicles”. *AIAA Paper 84-1730*, 1984.
- [22] J.P. Appleton and K.N.C. Bray. “The Conservation Equations for a Nonequilibrium Plasma”. *Journal of Fluid Mechanics*, 20(4):659–672, June 1964.
- [23] M. Mitchner and C.H. Kruger Jr. *Partially Ionized Gases*. Wiley, New York, 1973.
- [24] P.A. Gnoffo, R.N. Gupta, and J.L. Shinn. “Conservation Equations and Physical Models for Hypersonic Air Flows in Thermal and Chemical Nonequilibrium”. *NASA TP-2867*, Feb. 1989.
- [25] C. Park. “Rotational Relaxation of N<sub>2</sub> Behind a Strong Shock Wave”. *Journal of Thermophysics and Heat Transfer*, 18(4):527–533, Oct.-Dec. 2004.
- [26] M. Nishida and M. Matsumoto. “Thermochemical Nonequilibrium in Rapidly Expanding Flows of High-Temperature Air”. *Zeitschrift für Naturforschung, Teil A: Physik, Physikalische Chemie, Kosmophysik*, 52(4):358–368, 1997.
- [27] S.S. Lazdinis and S.L. Petrie. “Free Electron and Vibrational Temperature Nonequilibrium in High Temperature Nitrogen”. *Physics of Fluids*, 17(8):1539–1546, Aug. 1974.
- [28] J.H. Lee. “Electron-Impact Vibrational Relaxation in High-Temperature Nitrogen”. *Journal of Thermophysics and Heat Transfer*, 7(3):399–405, July-Sept. 1993.
- [29] C. Park and S.H. Lee. “Validation of Multitemperature Nozzle Flow Code”. *Journal of Thermophysics and Heat Transfer*, 9(1):9–16, Jan.-Mar. 1995.
- [30] E. Shima and K. Kitamura. “Parameter-Free Simple Low-Dissipation AUSM-Family Scheme for All Speeds”. *AIAA Journal*, 49(8):1693–1709, August 2011.
- [31] T.R.A. Bussing and E.M. Murman. “Finite-Volume Method for the Calculation of Compressible Chemically Reacting Flows”. *AIAA Journal*, 26(9):1070–1078, 1988.
- [32] Y. Takahashi, H. Kihara, and K. Abe. “The Effects of Radiative Heat Transfer in Arc-Heated Nonequilibrium Flow Simulation”. *Journal of Physics D: Applied Physics*, 43(18):185201, 2010.
- [33] K. Fujita and T. Abe. “SPRADIANT, Structured Package for Radiation Analysis: Theory and Application”. ISAS Report 669, Institute of Space and Aeronautics Science, Sagamihara, Japan, Sep. 1997.
- [34] K. Fujita, H. Takayanagi, T. Suzuki, T. Yanagisawa, H. Kurosaki, M. y Yamamoto, Y. Ishihara, and S. Abe. “Optical Tracking and Spectroscopic Measurement of Hayabusa Capsule Reentry Fireball”. *AIAA Paper 2011-140*, 2011.
- [35] R.L. Potts. “Application of Integral Methods to Ablation Charring Erosion, A Review”. *Journal of Spacecraft and Rockets*, 32(2):200–209, March-April 1995.
- [36] T. Suzuki and K. Fujita. “Post-Flight TPS Analysis of Hayabusa Reentry Capsule”. *AIAA Paper 2011-3759*, 2011.
- [37] I.D. Boyd, G. Chen, and G.V. Candler. “Predicting failure of the continuum fluid equations in transitional hypersonic flows”. *Physics of Fluids*, 7(1):210–219, 1995.

- [38] C.O. Johnston, B.R. Hollis, and K. Sutton. “Non-Boltzmann modeling for air shock-layer radiation at lunar-return conditions”. *Journal of Spacecraft and Rockets*, 45(5):879–890, 2008.
- [39] A. D’Angola, G. Colonna, C. Gorse, and M. Capitelli. “Thermodynamic and Transport Properties in Equilibrium Air Plasmas in a Wide Pressure and Temperature Range”. *The European Physical Journal D*, 46:129–150, 2008.